



Classification and snow line detection for glacial areas using the polarimetric SAR image

Lei Huang^a, Zhen Li^{a,*}, Bang-Sen Tian^a, Quan Chen^a, Jiu-Liang Liu^{a,b}, Rui Zhang^c

^a Center for Earth Observation and Digital Earth, Chinese Academy of Sciences, Beijing, China

^b Graduate University of Chinese Academy of Sciences, Beijing, China

^c Department of Geography and Geoinformation Science, College of Science, George Mason University, Fairfax, USA

ARTICLE INFO

Article history:

Received 19 August 2010

Received in revised form 3 March 2011

Accepted 4 March 2011

Available online 7 April 2011

Keywords:

Classification

Snow line

Polarimetric SAR

Support vector machines

Target decomposition

ABSTRACT

Snow cover and glaciers are sensitive indicators of the environment. The vast spatial coverage of remote sensing data, coupled with the tough conditions in areas of interest has made remote sensing a particularly useful tool in the field of glaciology. Compared to optical images, synthetic aperture radar (SAR) data are hardly influenced by clouds. This is important because glacial areas are usually under cloud cover. The Dongkemadi glacier in the Qinghai–Tibetan plateau was selected as the study area for this paper. We use polarimetric SAR (PolSAR) image for classification on and around the glacier. The contrast between ice and wet snow is remarkable, but it is difficult to distinguish the ice from the ground on SAR images due to similar backscatter characteristics in former research. In our study, we found that this distinction can be achieved by target decomposition. Support Vector Machines (SVMs) are performed to classify the glacier areas using the selected features. The glacial areas are classified into six parts: wet snow, ice, river outwash, soil land, rocky land and others. The PolSAR–Target decomposition–SVMs (PTS) method is proven to be efficient, with an overall classification accuracy of 91.1% and a kappa coefficient of 0.875. Moreover, 86.63% of the bare ice and 96.76% of the wet snow are correctly classified. The classification map acquired using the PTS method also helps to determine the snow line, which is an important concept in glaciology.

© 2011 Elsevier Inc. All rights reserved.

1. Introduction

Changes in glaciers, including snow and ice changes, are related to climate change and human life on the earth. For a long time, glaciers have been recognized as sensitive indicators of climate change (Konig et al., 2001a). The mass balance at the surface of a glacier (the gain or loss of snow and ice over a hydrological cycle) is determined by the climate (IPCC, 2007). Further, seasonal snow cover and alpine glaciers are critical to radiation and water balance (Shi & Dozier, 1995), and they are the main sources of water supply in many places of the world. In the field of glaciology, satellite remote sensing allows us to conduct research on remote areas that are hard to access, and to gather data on a spatial extent not possible by fieldwork alone. Optical images are usually used to determine the extent of snow or ice cover (Salomonson & Appel, 2004), however, they have some obvious disadvantages: 1, in mountainous glacier areas, optical images are often affected by clouds. On the southern part of the Qinghai–Tibetan plateau, which is strongly affected by monsoons, cloud cover is quite common, especially during the summer months. The progress of the Secondary Chinese Glacier Inventory is even hindered in these areas

due to a lack of cloud-free optical images; 2, an ambiguity between snow and ice exists because both have similar optical properties in glacial areas (Gupta et al., 2005); and 3, the mountain shadow makes it difficult to discriminate between glacier areas and non-glacier areas.

Regular and frequent mapping is necessary to monitor glaciers, and requires sensors that are time and weather independent. Synthetic aperture radar (SAR) provides an appropriate option. The strengths of SAR as a land observation tool are in the sensitivity of radar backscatter to the target media and all-weather, day or night imaging capability (Baghdadi et al., 1997). Detailed investigations have been carried out to learn about the possibility of SAR for snow and glacier applications (Rott & Mätzler, 1987). Theoretical work that focuses on understanding the backscattering coefficient from glaciers is well documented and supported by experimental data. In the low electromagnetic wave frequency, dry snow does not change the backscattering significantly compared to bare ground. When the snow is wet, however, the attenuation from the snow volume is the dominant effect, resulting in low backscattering (Malnes & Guneriusson, 2002). The difference between the bare-ice and wet-snow is distinctive, which allows the snow line to be determined. However, it is often difficult to discriminate glacial ice from the surrounding land using SAR data due to the fact that they have similar backscatter characteristics (Konig et al., 2001a). To distinguish glaciers from non-glaciers, optical images are added to complement SAR data (Jaenicke et al., 2006). Unfortunately, cloud is a

* Corresponding author at: Center for Earth Observation and Digital Earth, Chinese Academy of Sciences, Beijing 100094, China. Tel.: +86 10 82178159.

E-mail address: zli@irsa.ac.cn (Z. Li).

fatal problem for optical images, which was discussed earlier. Repeat pass SAR coherence was demonstrated to map snow covered areas (Shi et al., 1997; Strozzi et al., 1999). In our research, we attempted to combine the L-band SAR coherence image to the polarimetric SAR (PolSAR) feature space to discriminate glaciers from non-glaciers. However, the registration between SAR images of different sensors is quite difficult in mountainous areas.

Compared to conventional single-channel SAR, the inclusion of SAR polarimetry can provide a significant improvement in the quality of the data analysis (Shimoni et al., 2009). Airborne experiments prove that multipolarization SAR is a better tool for glacier monitoring than previous single polarization SAR sensors (Rott & Davis, 1991; Rott et al., 1992; König et al., 2001b). The performance of different PolSAR features for land cover classification was reviewed in (Shimoni et al., 2009). In our study, target decomposition was applied on the polarimetric SAR images to investigate more information. Our experiments proved that target decomposition provides sufficient features for classification in glacial areas.

Recent developments in land cover classification of remote sensing images were, to a great extent, driven by two important factors: the increased availability of data, and the shift from statistical approaches to more powerful and flexible machine learning algorithms for data classification (Waske & Linden, 2008). To properly exploit SAR data in multiclass classification problems, we need to develop a system based on: 1, effective feature-extraction procedures and, 2, an appropriate classification method that takes into account the peculiarities of currently available SAR signals. The support vector machines (SVMs) are a group of theoretically superior machine learning algorithms, which are excellent in terms of computational cost, accuracy, and robustness compared to common levels of noise (Camps-Valls & Bruzzone, 2005; Huang et al., 2002). In this paper, the PolSAR target decomposition features in conjunction with the SVMs method, called the PTS method, is used to make ground cover classification in glacial areas. Further, the PTS provides an accurate way to identify the snow line of the glaciers.

2. Study area and data

This study was performed around the Dongkemadi glacier (as shown in Fig. 1), which lies in the eastern part of the Qinghai-Tibetan plateau. The Dongkemadi glacier consists of a main glacier, which is called the Da-Dongkemadi (DD) glacier, and a branch glacier, which is called the Xiao-Dongkemadi (XD) glacier. The altitude of the DD glacier ranges from 5275 to 6060 m, and on the XD glacier the altitude ranges from 5380 to 5926 m. The lengths of the DD glacier and the XD glacier are 5.4 km and 2.8 km, respectively. The terrain of the two glaciers is relatively gentle. Mass balance data from 1989 were recorded on the Dongkemadi glacier (Fujita et al., 2000). The warm season in the study area, when most of the yearly precipitation falls in the form of snow, spans from June to September every year. According to fieldwork, the land cover can be classified into five types: wet snow, ice, river outwash, rocky land and soil land with sparse low-growing grass. These types are shown in Fig. 2. On the SAR images, there is a special, high brightness type called natural corner reflector (NCR, which is formed by the structure of the glacier). The natural corner reflector is not a kind of land cover object but rather a natural structure, as shown in Fig. 2a. The characteristic of the structure will be introduced below. The NCR is listed as an independent type to avoid mis-classification of the other types.

The C-band RADARSAT-2 quad-polarization SAR data is used in this study. The RADARSAT-2 image is acquired in late summer, and the specific parameters are listed in Table 1.

Digital Elevation Model (DEM) data are necessary to check the snow line altitude on the images and the Shuttle Radar Topography Mission (SRTM) DEM are used for this study. The spatial posting of the employed DEM is 90 m, and the 90% height error for Eurasia is given as 8.7 m (Rodriguez et al., 2006).

3. Methods

3.1. Target decomposition

An important objective of target decomposition is to extract physical information from the observed scattering of microwaves by both surface and volume structures. It is important to understand the average, or dominant, scattering mechanism for the purpose of classification (Cloude & Pottier, 1996). In this paper, both Pauli and $H/A/\bar{\alpha}$ decomposition are employed. The parameters that are extracted from the target decomposition will be used to build the feature space for further classification.

3.1.1. Pauli decomposition

Pauli decomposition expresses the scattering matrix $[S]$ as the complex sum of the Pauli matrices, where an elementary scattering mechanism is associated with each basis matrix:

$$S = \begin{bmatrix} S_{HH} & S_{HV} \\ S_{VH} & S_{VV} \end{bmatrix} = \frac{a}{\sqrt{2}} \begin{bmatrix} 1 & 0 \\ 0 & 1 \end{bmatrix} + \frac{b}{\sqrt{2}} \begin{bmatrix} 1 & 0 \\ 0 & -1 \end{bmatrix} + \frac{c}{\sqrt{2}} \begin{bmatrix} 0 & 1 \\ 1 & 0 \end{bmatrix} + \frac{d}{\sqrt{2}} \begin{bmatrix} 0 & -j \\ j & 0 \end{bmatrix} \quad (1)$$

where a , b , c and d are all complex and given by:

$$a = \frac{S_{HH} + S_{VV}}{\sqrt{2}}, b = \frac{S_{HH} - S_{VV}}{\sqrt{2}}, c = \frac{S_{HV} + S_{VH}}{\sqrt{2}}, d = j \frac{S_{HV} - S_{VH}}{\sqrt{2}} \quad (2)$$

In the monostatic case, where $S_{HV} = S_{VH}$, the Pauli matrix basis can be reduced to the first three matrices, which leads to $d = 0$ (Lee & Pottier, 2009). It follows that the Span value is given by:

$$\text{Span} = |S_{HH}|^2 + 2|S_{HV}|^2 + |S_{VV}|^2 = |a|^2 + |b|^2 + |c|^2 \quad (3)$$

The application of Pauli decomposition to deterministic targets may be considered the coherent composition of three scattering mechanisms: $|a|^2$ determines the power scattered by the targets characterized by single- or odd-bounce; $|b|^2$ determines the power characterized by double- or even-bounce; $|c|^2$ determines the power characterized by a diplane oriented at 45° . From a qualitative point of view, the scattering mechanism represented by $|c|^2$ refers to those scatters that are able to return an orthogonal polarization. One of the best examples of this is the volume scattering produced by the forest canopy.

3.1.2. $H/A/\bar{\alpha}$ decomposition

This method relies on an eigenvalue analysis of the coherency matrix, $\langle T \rangle$, and it employs a three-level Bernoulli statistical model to general estimates of the average target scattering matrix parameters from the data. Applying eigenvalue analysis, the $\langle T \rangle$ matrix is decomposed into

$$\langle T \rangle = \lambda_1 e_1 e_1^{*T} + \lambda_2 e_2 e_2^{*T} + \lambda_3 e_3 e_3^{*T} \quad (4)$$

where λ_i and e_i are the eigenvalues and eigenvectors, respectively. The eigenvectors can be written as

$$e_i = e^{i\phi_i} \begin{bmatrix} \cos \alpha_i & \sin \alpha_i \cos \beta_i e^{i\phi_i} & \sin \alpha_i \sin \beta_i e^{i\phi_i} \end{bmatrix}^T \quad (5)$$

The parameter $\bar{\alpha}$ which corresponds to the mean target power is defined by

$$\bar{\alpha} = \sum_{k=1}^3 P_k \alpha_k, \text{ where } P_k = \frac{\lambda_k}{\sum_{j=1}^3 \lambda_j} \quad (6)$$

The average of α is defined as

$$\bar{\alpha} = P_1 \alpha_1 + P_2 \alpha_2 + P_3 \alpha_3 \quad (7)$$

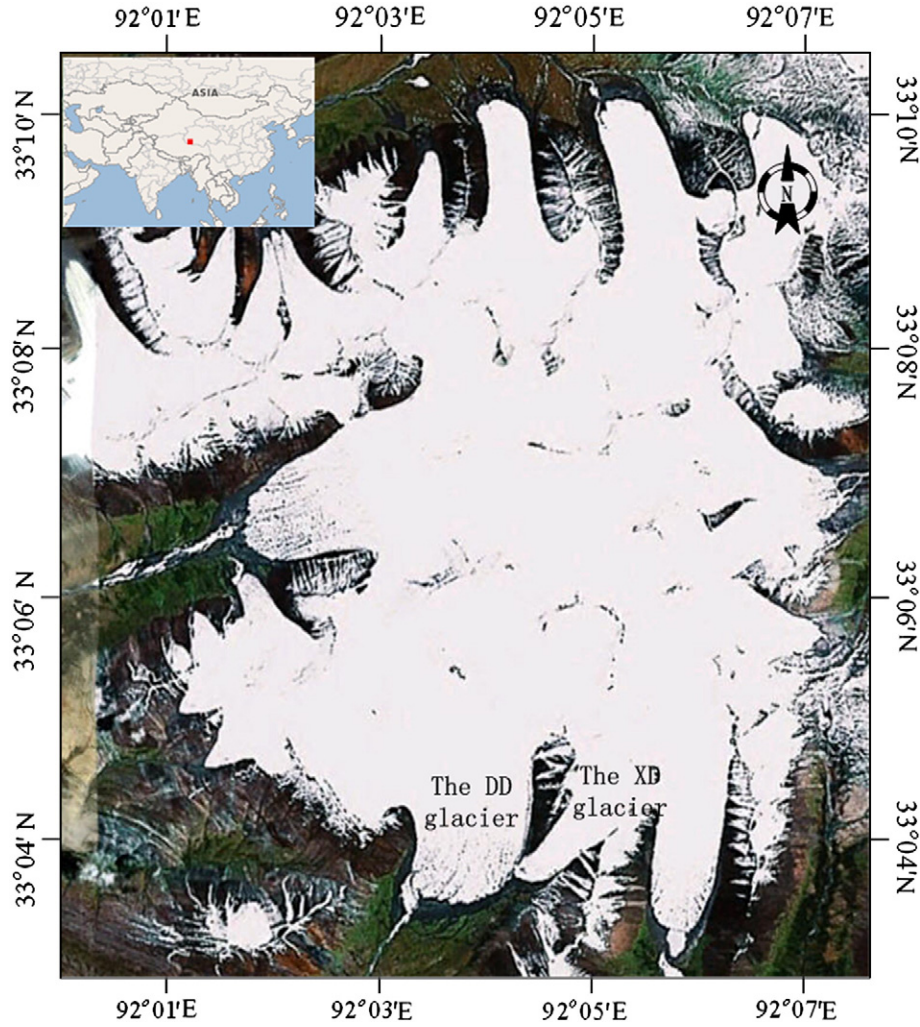


Fig. 1. The study area around the Dongkemadi glacier acquired from Google Earth (the original image is acquired in May, 2009, from Spot 5). The map on the top left corner shows the relative location of the glaciers within Asia.

The main parameter for identification of the dominant scattering mechanism is $\bar{\alpha}$, which is a roll-invariant parameter. This angle has a useful range of 90° and corresponds to a continuous change from surface scattering ($\bar{\alpha} = 0^\circ$) to dipole scattering ($\bar{\alpha} = 45^\circ$) to double bounce scattering from conductive surfaces ($\bar{\alpha} = 90^\circ$).

In order to define the degree of statistical disorder for each distinct scatter type within the ensemble, the polarimetric entropy H , provides an efficient and suitable basis-invariant parameter.

$$H = - \sum_{k=1}^3 P_k \log_3(P_k) \quad (8)$$

The entropy, ranging from 0 to 1, represents the randomness of the scattering medium from isotropic scattering ($H=0$) to totally random scattering ($H=1$) (Lee et al., 1999). The scattering entropy is a key parameter in determining the randomness in this model and is seen as a fundamental parameter in assessing the importance of polarimetry in remote sensing problems (Cloude & Pottier, 1997).

The polarimetric anisotropy, A , is a complementary parameter to the polarimetric entropy H (Pottier & Lee, 1999).

$$A = \frac{\lambda_2 - \lambda_3}{\lambda_2 + \lambda_3} \quad (9)$$

The anisotropy measures the relative importance of the second and the third eigenvalues of the eigen-decomposition. The polarimetric

anisotropy, A , is a very useful parameter and plays a key role in improving the capability of distinguishing different types of scattering processes when the polarimetric entropy, H , reaches a high value (Lee & Pottier, 2009).

3.2. Support vector machines

The SVMs method is a non-parametric approach based on the statistical learning theory (Vapnik, 1995). For a given training sample belonging to two different classes, Support Vector Machines derives a hyperplane that is at a maximum distance from the closest points belonging to both classes. Supposing that the training set consists of n samples from a d dimensional feature space, $x_i \in \mathbb{R}^d$ ($i = 1, 2, \dots, n$). A target $y_i \in \{-1, +1\}$ is associated with each training pattern x_i . Under the condition that the two classes are linearly separable, the SVMs approach formulates the optimization problem as

$$\begin{cases} \max : \sum_{i=1}^n \alpha_i - \frac{1}{2} \sum_{i=1}^n \sum_{j=1}^n \alpha_i \alpha_j y_i y_j (x_i \cdot x_j) \\ \text{subject to : } \sum_{i=1}^n \alpha_i y_i = 0, \alpha_i \geq 0, i = 1, 2, \dots, n. \end{cases} \quad (10)$$

The discriminant function associated with the optimal hyperplane is

$$f(x) = \sum_{i \in SV} \alpha_i y_i (x_i \cdot x) + b \quad (11)$$

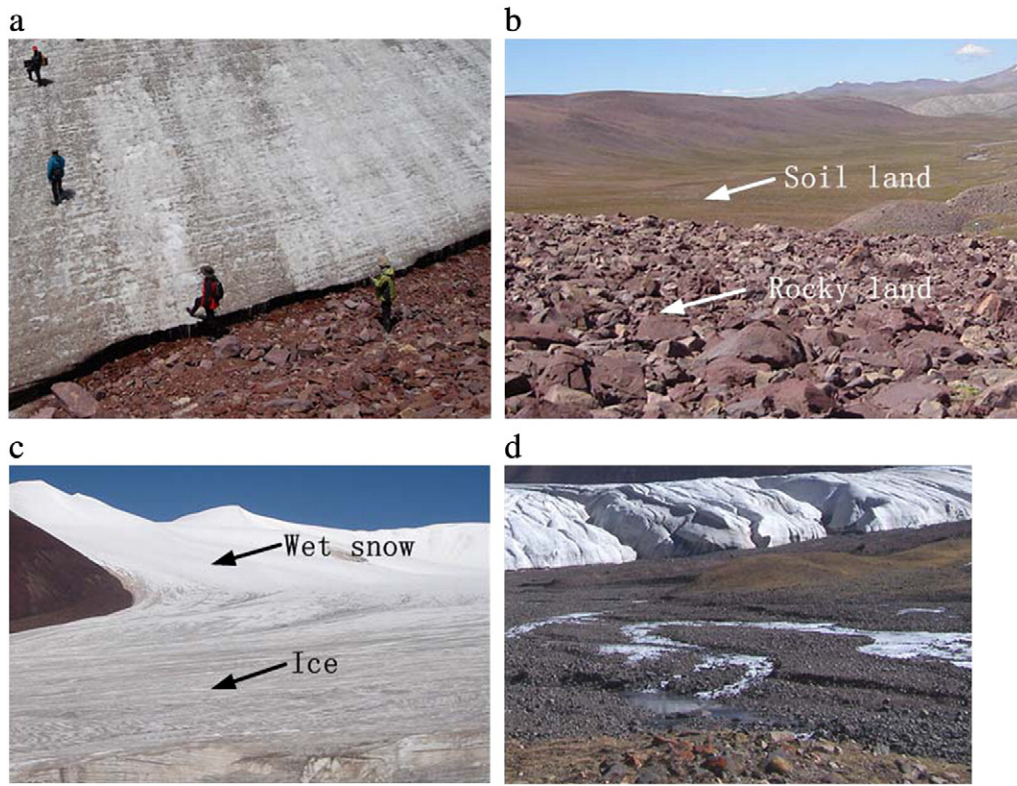


Fig. 2. Field photos taken around the Dongkemadi glacier. (a) The steep edge of the glacier that forms the NCR. (b) Soil land and rocky land. (c) Wet snow and ice on the glacier surface. (d) The river outwash at the terminus of the glacier.

where SV is the subset of training samples corresponding to the nonzero Lagrange multipliers α_i . These training samples are called SVs.

For the nonlinear case, we may solve the problem in a certain high-dimensional space using a kernel map $\Phi(\cdot)$. The problem then becomes:

$$\begin{cases} \max : \sum_{i=1}^n \alpha_i - \frac{1}{2} \sum_{i=1}^n \sum_{j=1}^n \alpha_i \alpha_j y_i y_j \Phi(x_i) \cdot \Phi(x_j) \\ \text{subject to : } \sum_{i=1}^n \alpha_i y_i = 0, \quad 0 \leq \alpha_i \leq C, i = 1, 2, \dots, n. \end{cases} \quad (12)$$

where $\Phi(x_i) \cdot \Phi(x_j) = K(x_i, x_j)$. That is, the dot product in the high dimensional space is equivalent to a kernel function of the input space. The parameter C is used to penalize the data points that cross the boundaries (Chen et al., 2009), and good results were achieved in the range of $C \in [1-100]$ in other research (Camps-Valls et al., 2004). Accordingly, the discriminant function becomes

$$f(x) = \sum_{i \in SV} \alpha_i y_i K(x_i, x) + b \quad (13)$$

A widely used kernel in remote sensing applications is the Gaussian RBF kernel:

$$K(x_i, x_j) = \exp(-\gamma \|x_i - x_j\|^2) \quad (14)$$

Multi-class SVMs are usually implemented by combining several two-class SVMs. Here, we used the 'one-against-one' (OAO) approach for multi-class cases.

4. Experiments and analyses

The RADARSAT-2 PolSAR image is processed in the following procedure: First, a multi-look image with 2 looks in the azimuth direction and 1 look in the range direction is generated, and the absolute calibration is performed (RSI, 2000) second. A refined Lee Sigma filter is used to suppress speckle noise (Lee et al., 2009), and then target decomposition is performed. Next, the SVMs and other classifiers are used for image classification. Following this procedure, a control points (CPs) based geo-rectification is performed on the classification map for land cover mapping and snow line detection. The control point pairs are selected on the PolSAR image and the optical ortho-image, and the polynomial transformation parameters are calculated using these CPs. Finally, the parameters are used to warp the classification map. Some authors made geo-rectification on original SAR image before classification (Adam et al., 1997), which may be more accurate. However, we think that pixel resampling during the process of geo-rectification reduces the image quality, which further influences the quality of classification. In this paper, therefore, SAR image geo-rectification is made after classification.

In high relief areas, the angular normalization of SAR backscatter was made for inversion or other use (Lee et al., 2000). However, radiometric terrain correction of the employed image is not made here because of

Table 1
SAR satellite data used in this study.

Date	Pass direction	Acquisition type	Product type	Nominal pixel spacing (range \times azimuth) (meters)	Range of incidence angle (degrees)	Image ID
Aug 30, 2009	Ascending	Fine quad polarization	SLC	4.7×5.1	18–49	50341

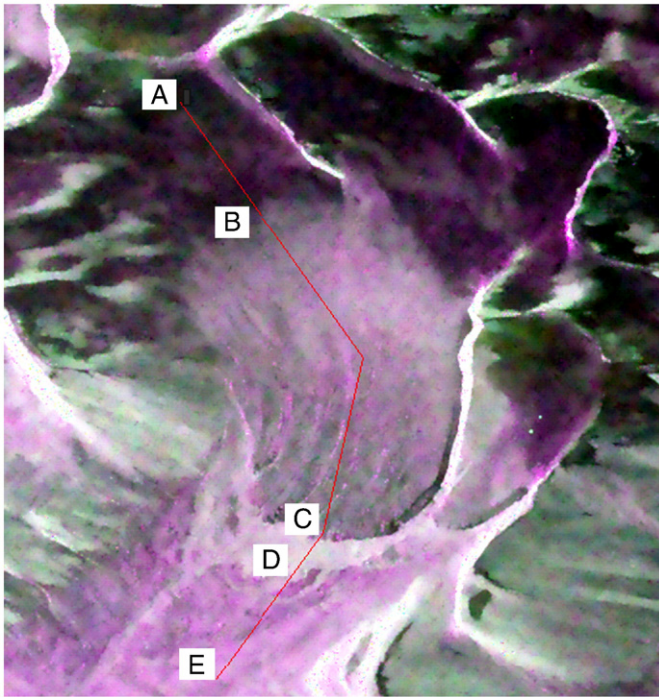


Fig. 3. The centerline of the DD glacier. The base image is the polarimetric SAR data. HH: red, HV: green, and VV: blue.

the low resolution of the employed DEM (90 m), which gives little help in relief areas. Fortunately, most of the glacial areas are relatively gentle, and the small amounts of steep areas are taken as a special class NCR to reduce the terrain influence.

4.1. Polarimetric information analysis

As mentioned previously, ice is distinct from wet snow, but it is easily confused with the ground on polarimetric SAR image. Therefore, in this section we will focus on how to differentiate the ice from the ground. The centerline of the DD glacier is presented in Fig. 3. Along the centerline, the glacier is divided into four parts using five points, A, B, C, D and E according to the changes on the image. The line segment AB passes through wet snow, BC passes through bare ice, CD passes through river outwash and DE passes through soil land.

Absolute calibration and noise filters are applied to the PolSAR image to permit quantitative analysis of the spatial variation of the

backscattering signal (σ^0). The backscattering coefficients along the centerline of the DD glacier are shown in Fig. 4. The co-polarized signature (HH and VV) is similar, and the cross-polarized signature (HV = VH) is, on average, 10 dB lower. AB represents the wet snow facies with a very low backscattering coefficient. At C-band, the main components of the SAR backscattering signal are snow volume-backscattering and surface backscattering from the air–snow interface (Shi & Dozier, 1995). The lower values during wet snow conditions are due to increased attenuation by the snow cover when the surface of the snow is relatively smooth. Generally, backscattering from wet snow is dominated by surface scattering at small incidence angles and by volume scattering at large incidence angles (Baghdadi et al., 1998). BC runs through the bare ice facies, which has backscattering coefficients about 10 dB higher than wet snow in both co-polarization and cross-polarization. Because it is a specular reflector, the smooth ice surface causes lower backscatter than the wet snow facies in winter. In summer, however, the backscatter of the bare ice facies appears higher due to the presence of melt and the low backscatter in the wet snow facies. CD runs through the river outwash at the terminus of the glacier. According to observations made in the field, the river outwash is a mixture of river, gravel and small amount of ice. The cross-polarization is obviously high in this area, due to the coarse surface that causes multi-scattering. Over a wider extent, the backscattering coefficient of the river outwash fluctuates widely because the river outwash facies is unevenly distributed. DE is drawn through the ground that is composed of the soil and the low grass facies. The backscattering coefficient values along DE are close to those seen on BC, which makes them difficult to separate.

In summary, if we look solely at the backscattering coefficient, the wet snow is distinct, but it is hard to tell the difference between the ice and the ground in glacial areas. Thus, we try to use target decomposition to find the difference between these kinds of facies. Target decomposition aims to provide a physical interpretation to help understand and classify PolSAR images.

Target decomposition provides useful information along the centerline of the glacier. In the wet-snow areas between AB, the three scattering components are obviously lower than other areas shown in Fig. 5a, and this corresponds to the low target power λ in Fig. 5b. This difference is caused by the strong attenuation of wet snow when the surface of the snow cover is smooth. Between A and B, the three scattering components are evenly distributed and the average difference value is about 5 dB (Fig. 5a). This explains the high entropy and anisotropy values in Fig. 5b. In Fig. 5c, the average α value between A and B is 28.5° , which is higher than what is seen in other areas. This difference implies that this area has impure surface scattering but is close to volume scattering. The average α value of the river outwash area, CD, is very close to AB. In contrast, the ground area DE shows an

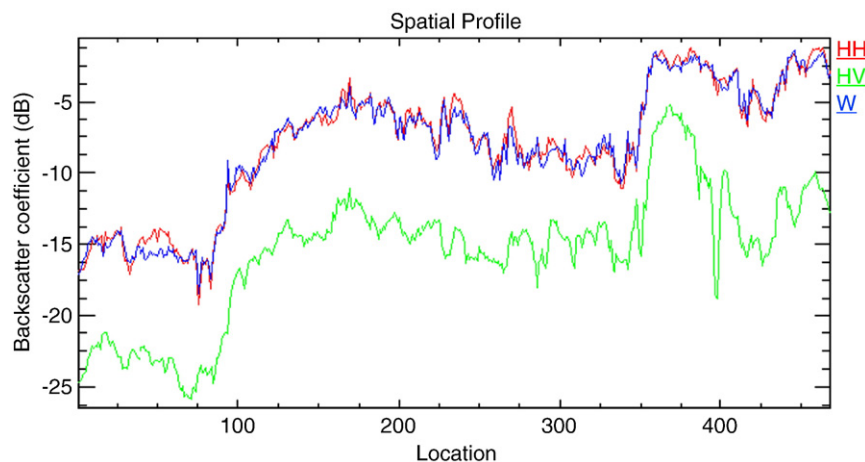


Fig. 4. The backscattering coefficient along the centerline of the DD glacier. The points A–E corresponds to A–E in Fig. 3.

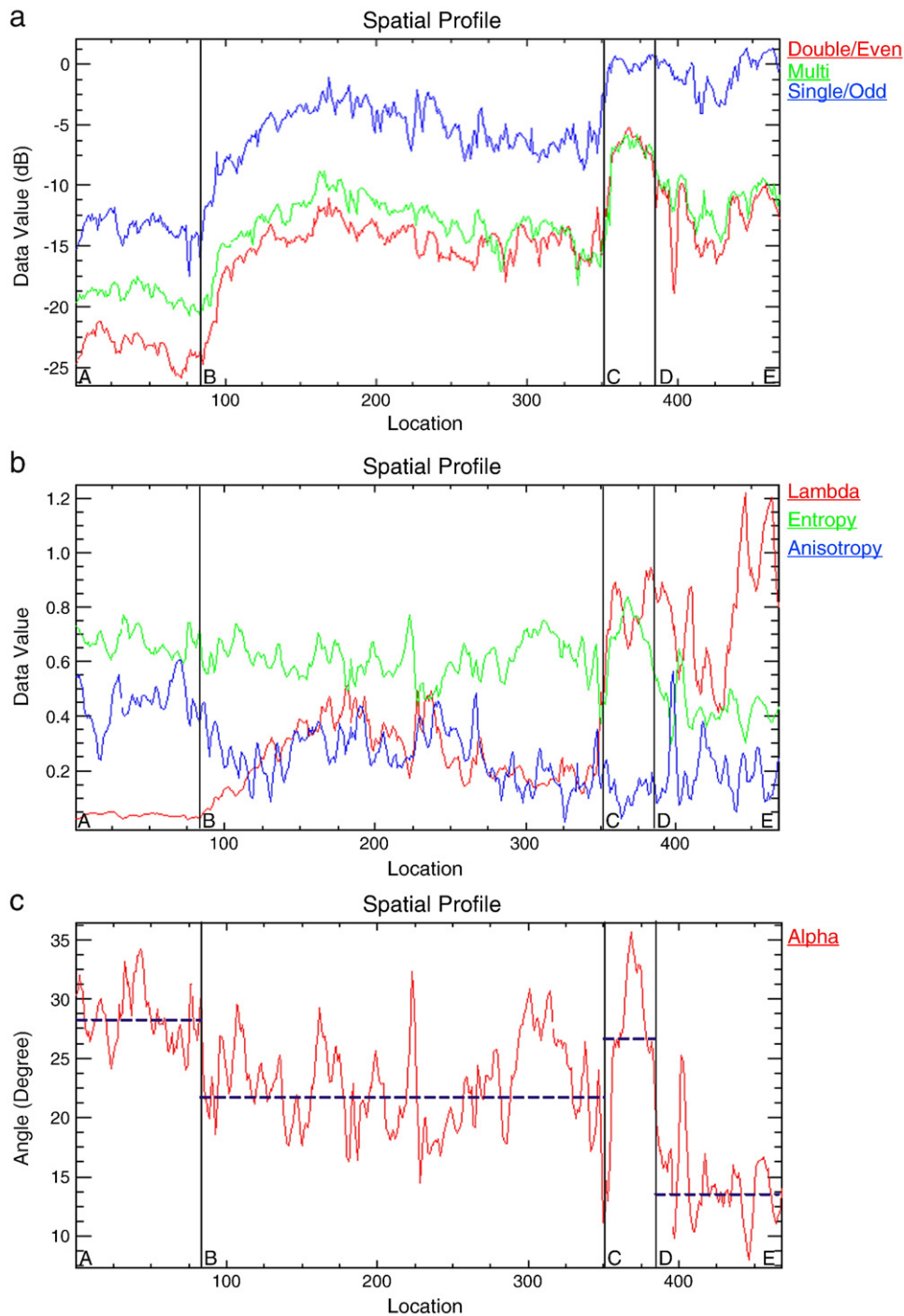


Fig. 5. The target decomposition results along the centerline. a. Pauli decomposition; b and c are $H/A/\bar{\alpha}$ target decomposition. The points A–E corresponds to A–E in Fig. 3. The blue dotted lines show the average values for the four zones. Lambda, entropy, anisotropy and alpha correspond to the parameters $\bar{\lambda}$, H , A and $\bar{\alpha}$ in the $H/A/\bar{\alpha}$ decomposition.

obvious difference, which implies that DE is dominated by surface scattering. The ice area along BC lies between these two cases.

The separation between BC (ice) and DE (soil land) can be understood using three features: entropy (H), lambda ($\bar{\lambda}$) and alpha ($\bar{\alpha}$). First, the average entropy between B and C is 0.59 while the average entropy between D and E is 0.42. In Fig. 5a, the gap between single/odd bounce and the other two scattering components of BC is smaller than that along DE; this is the reason that the entropy along BC is higher. Second, despite irregular fluctuations, the average $\bar{\lambda}$ value between D and E is higher than that along BC. This is shown in Fig. 5b. and implies that the mean backscattering power from the ground is higher than the ice in this area. Third, the $\bar{\alpha}$ value between B

and C is 22° , whereas it is 13° between D and E. $\bar{\alpha}$ corresponds to a continuous change from surface scattering ($\bar{\alpha} = 0^\circ$) to dipole scattering ($\bar{\alpha} = 45^\circ$). These results show that surface scattering is the dominant component on the soil, but that its contribution is lower on the ice. This conclusion can also be validated using Pauli decomposition, as shown in Fig. 5a.

Outside the centerline, there are two different kinds of ground objects in the study area that have been previously introduced: the natural corner reflector and the rocky land. Strictly speaking, the natural corner reflector is not a ground object, but rather it is a special structure formed by the ground and relief glacier edge facing the satellite. On the SAR image, it is completely distinct from other objects

due to strong backscattering intensity, and thus it is listed as a special object. The rocky land is also easily distinguished using $H/A/\bar{\alpha}$ decomposition features because its surface is the roughest of the six kinds of objects. The average entropy and $\bar{\alpha}$ values of the rocky land samples are 0.829 and 36.907, respectively, which are both the highest of the six land cover types except the NCR. These results indicate that the scattering mechanism is diverse on the rocky land, and that there is no longer a single equivalent point scatterer.

To more easily compare the six kinds of ground objects, we normalized the data values and plotted them together in different feature space, as seen in Fig. 6. In each feature, the pixel values are normalized using the following equation:

$$I_{(i,j)}^m = \frac{O_{(i,j)}^m - \text{Min}^m}{\text{Max}^m - \text{Min}^m} \quad (15)$$

where m is the feature space index, (i, j) is the pixel index, $I_{(i,j)}^m$ is the new value of a pixel in feature m , $O_{(i,j)}^m$ is the original value of the pixel in feature m . Max^m is the maximum value and Min^m is the minimum value in feature m . The features which range between $[0, 1]$ in their raw forms, such as the entropy and the anisotropy, are not involved in the normalization with Eq. (15). The average values and the standard deviation of the six ground objects are calculated respectively, using the training sets in Fig. 7a.

In each feature, there are overlapping areas between different kinds of objects. This overlap is the reason for most misclassifications in usual cases. The backscattering coefficient and Pauli decomposition features for the wet snow and the natural corner reflector are distinct in all of the feature spaces, while the other four objects heavily overlap. Five of the six ground objects (except the river outwash) are distinct from other objects in at least one feature space when looking at the features from the $H/A/\bar{\alpha}$ decomposition, which will greatly helps further classification. Theoretical analyses were performed to understand the scattering mechanism in the glacial areas and to support the experiments. We used the results of the work on the radar backscattering/glacier surface interaction and then concentrated on digital mapping of the detectable glacier facies.

4.2. Classification

In this section, we combine the feature space and the classifier together to perform the final classification. The SVMs classifier is done using the C++ language and the LibSVM (Hsu et al., 2009). The RBF kernel is employed, and the penalty parameter C and the parameter γ in the RBF kernel function are selected according to 5-fold cross-validation.

The following experiments are made using the same training sets and testing sets, as shown in Fig. 7. The ground truth points were determined from fieldwork and optical images. At first, the image is classified based on three groups of features: the backscattering coefficient, the Pauli decomposition and the $H/A/\bar{\alpha}$ decomposition parameters, using the same SVMs method. The accuracy assessments are listed in Tables 2–4 to quantify the performance of the three groups of features.

The features from the $H/A/\bar{\alpha}$ decomposition have the best performance in overall accuracy, kappa coefficient and nearly each class among the three groups of features. The four classes of wet snow, soil land, rocky land, and natural corner reflector are highly accurate for all three groups of features using the SVMs. The natural corner reflector is so distinct that it is completely distinguished from other facies. The accuracy of the ice classification is relatively lower using SVMs, but the accuracy increases about 10% by using the $H/A/\bar{\alpha}$ decomposition technique, compared to using the backscattering coefficient. The river outwash facies obtains the lowest accuracy of the six classes, only 63.74% of it is recognized, even when using the $H/A/\bar{\alpha}$ decomposition. As mentioned previously, the river outwash is a mixture of river, gravel and small amount of ice, so the scattering mechanism is the most complicated of all the facies. These results agree with our analysis in Section 4.1, that the river outwash is the only class that is not distinct in any of the feature spaces. Because the SVMs method has the ability to handle high-dimensional feature spaces, we tried to combine the features from the Pauli decomposition with the features from the $H/A/\bar{\alpha}$ decomposition. However, the accuracy (overall accuracy = 90.64%, kappa coefficient = 0.8688) did not increase with the number of features compared to the results of only using the features from the $H/A/\bar{\alpha}$ decomposition.

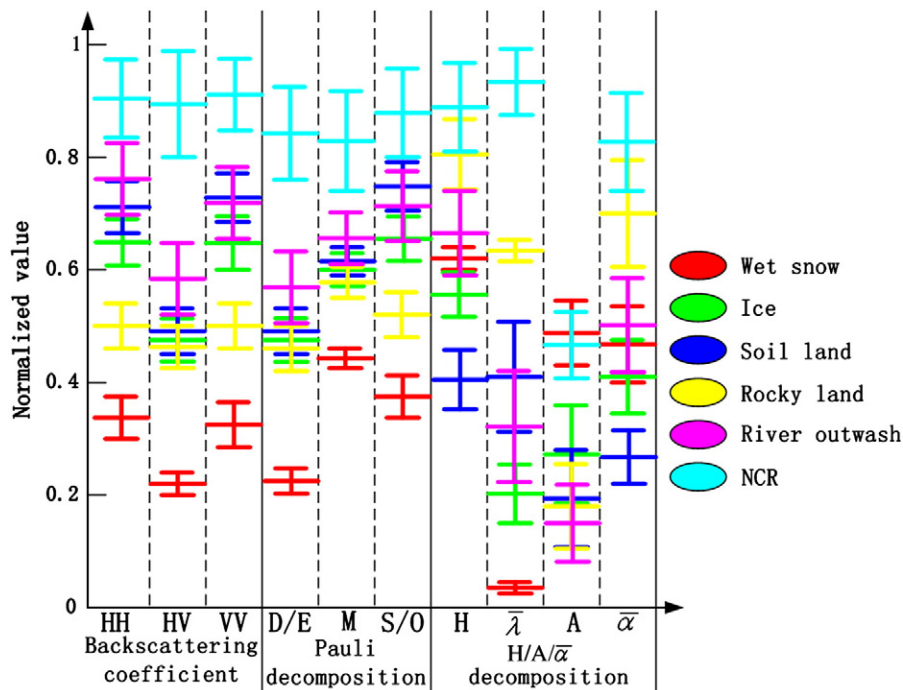


Fig. 6. The distribution of the six ground objects in different feature spaces. The average value and standard deviation of different objects are represented using the symbol. In the symbol, the middle line represents the average value, the distance between the top line (or the bottom line) and the middle line is the standard deviation.

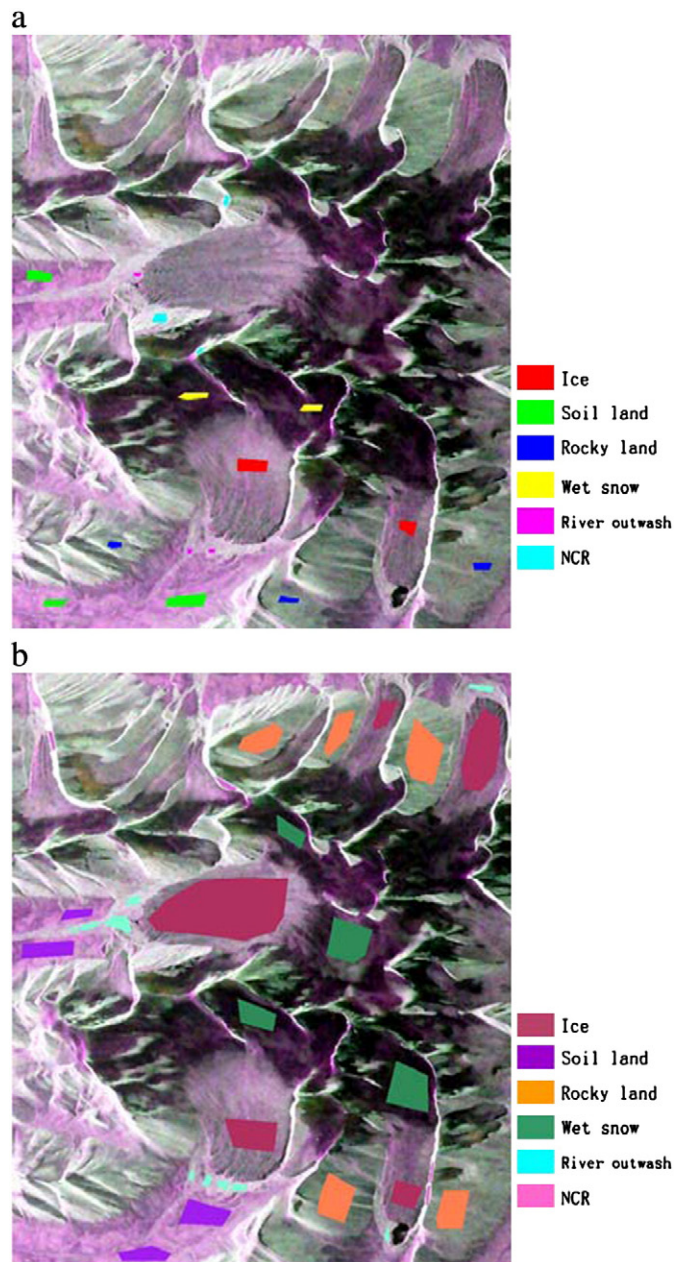


Fig. 7. (a) The training sets. (b) The testing set. The base image is the polarimetric SAR data. HH: red, HV: green, and VV: blue. The total training points are 10,331 and the total testing points are 110,094.

Table 2

The confusion matrix for classification using backscattering coefficients. Statistics are given in percentage of pixels for each theoretical class (rows: ground truth; columns: the detected class).

Class	Ice %	Wet snow %	Soil land %	Rocky land %	NCR ^a %	River outwash %
Ice	76.55	4.69	6.75	2.5	0	17.85
Wet snow	0.22	94.98	0	0.11	0	0
Soil land	3.86	0.31	92.27	0	1.6	5.23
Rocky land	19.36	0.02	0	97.39	0.25	2.02
NCR	0	0	0.02	0	97.89	20.22
River outwash	0.01	0	0.96	0	0.25	54.69

Overall accuracy = 85.19% (93,788/110,094), kappa coefficient = 0.7941.

^a NCR = Natural corner reflector.

Table 3

The confusion matrix for classification using Pauli decomposition features.

Class	Ice %	Wet snow %	Soil land %	Rocky land %	NCR %	River outwash %
Ice	82.77	3.29	5.57	2.02	0.08	13.89
Wet snow	0.08	96.12	0	0	0.08	0
Soil land	4.07	0.56	93.82	0	1.6	4.22
Rocky land	13.08	0.03	0	97.98	0	3.42
NCR	0	0	0.01	0	97.72	19.83
River outwash	0	0	0.6	0	0.51	58.65

Overall accuracy = 88.69% (97,637/110,094), kappa coefficient = 0.8417.

To test the performance of different classifiers, we classified the image using the same $H/A/\alpha$ decomposition features. We compare to two widely used classifiers, the Maximum Likelihood and the Decision Tree method, to examine the accuracy of the SVMs method. The results are shown in Table 5.

It is clear from Table 5 that the SVMs method has a higher overall accuracy and kappa coefficient than the other two methods. Conventional classification algorithms that assume certain statistical distributions of the training data are, therefore, not appropriate for solving the problem at hand. In contrast, the SVMs method attempts to separate samples belonging to different classes by tracing maximum margin hyperplanes in the kernel space where samples are mapped, and it does not rely on a supposed distribution of the samples.

According to the experiments, the $H/A/\alpha$ decomposition features and the SVMs classifier each had the best performance, respectively. In the next step, we will test the combined performance. A combination of backscattering coefficient with the decision tree is also used in the experiment. We make a comparison between the two combinations. In our experiment, the combination of backscattering coefficient and the decision tree has an overall accuracy of 66.23% and a kappa coefficient of 0.597, which is much lower than what is found with the combination of the $H/A/\alpha$ decomposition and the SVMs (overall accuracy = 91.10%, kappa coefficient = 0.875). Further, in the combination of backscattering coefficient analysis and the decision tree, only 62.6% percent of the ice can be correctly recognized, while the corresponding value is 86.63% for the combination of the $H/A/\alpha$ decomposition and the SVMs. Another problem that is present when using the decision tree is that it is time-consuming to select the threshold between different classes by hand. This manual selection may also lead to different results being obtained by different people. The study area covers about a dozen glaciers, therefore the performance of the combination of the $H/A/\alpha$ decomposition and the SVMs is likely robust for glacial area classification. The classification map using the $H/A/\alpha$ decomposition and the SVMs is shown in Fig. 8.

The common disadvantages of SAR images, such as foreshortening, speckle, and shadows are inevitable when using this method, and they contribute to a reduction of the final classification accuracy. Although the natural corner reflector is easily detected on the image, it provides no help for land cover mapping. The shadow area is another potential factor that may influence the final classification accuracy, but it is fortunately not serious within the study area due to the relatively gentle terrain. If shadows cover a large ratio on the SAR image, it might be

Table 4

The confusion matrix for classification using $H/A/\alpha$ decomposition features.

Class	Ice %	Wet snow %	Soil land %	Rocky land %	NCR %	River outwash %
Ice	86.63	2.68	3.27	1.35	0	13.04
Wet snow	1.56	96.76	0	0.47	0	0
Soil land	4.29	0.42	96.33	0	0	2.5
Rocky land	7.5	0.13	0	98.18	0	4.29
NCR	0	0	0	0	100	16.43
River outwash	0.02	0	0.4	0	0	63.74

Overall accuracy = 91.10% (100,294/110,094), kappa coefficient = 0.875.

Table 5

A comparison of the different classifiers.

Classifier	Overall accuracy	Kappa coefficient
Decision tree	0.8323	0.787
Maximum likelihood	0.854	0.806
SVM	0.91	0.875

necessary to list the shadow as a special type to avoid misclassification, just as the NCR has been listed.

There is another special problem for SAR images while they are used for classification in glacier areas: some small glaciers may disappear on the classification map. By comparing the classification map with the optical image, we find that some small glaciers are more easily misclassified than bigger glaciers. The reason is that small glaciers which lie in the narrow valley are more easily to be influenced by shadows and layovers. Compared to optical images, the advantage and disadvantages of the SAR images are all evident, and our work tries to extend the classification ability within these limitations.

4.3. Snow line detection

Forster and others define four radar glacier zones that they found on the temperate HPS by comparing C- and L-band imagery from space-shuttle missions. These zones are comprised of a relatively-dry snow zone, a moderately-wet snow zone, a wet snow zone (with weak returns in both bands) and a bare-ice zone (with strong returns in both bands) (Forster et al., 1996). In late summer, only two glacier facies can

be observed on Dongkemadi: the wet snow zone and the bare ice zone. This is typical for temperate glaciers (Jaenicke et al., 2006).

To better explain our work, it is necessary to make clear some key definitions in glaciology. In this paper, the snow line is defined as the transient boundary of wet snow and ice on a glacier (Adam et al., 1997). Similar to Forster and others definition of glacier zones (Forster et al., 1996), the snow line works on a timescale of days and weeks, rather than an annual timescale. In contrast, the firn line is the boundary between glacier ice and old firn from many previous years. In general, the firn line maintains a more stable position than the transient snow line, because of higher densification of the snowpack and thus lower melt rates (Jaenicke et al., 2006). In contrast to our definition, some authors use the terms firn line and snow line interchangeably (Paterson, 1994). The equilibrium line is another important concept, and it is defined as the boundary between the regions of net accumulation and net ablation (Nolin & Payne, 2007). The firn line is not affected by yearly variations in the equilibrium line altitude; however, a permanent change in the average equilibrium line altitude will eventually result in a change in the firn line. The firn line therefore seems to smooth out short-term variations and to show trends of larger time-scales. (Konig et al., 2001a). Now it is clear that the snow line, the equilibrium line and the firn line all reflect a glacier's status, but they work on different timescale.

In the past, boundaries were found on single channel SAR images from other glaciers, and they were interpreted to be the equilibrium lines (Engeset & Weydahl, 1998). However, most of these studies lack ground observations, and recent work suggests that (in many cases) these studies have identified the firn line rather the equilibrium line (Konig et al., 2001a). Since the C-band SAR signal is able to transmit through dry

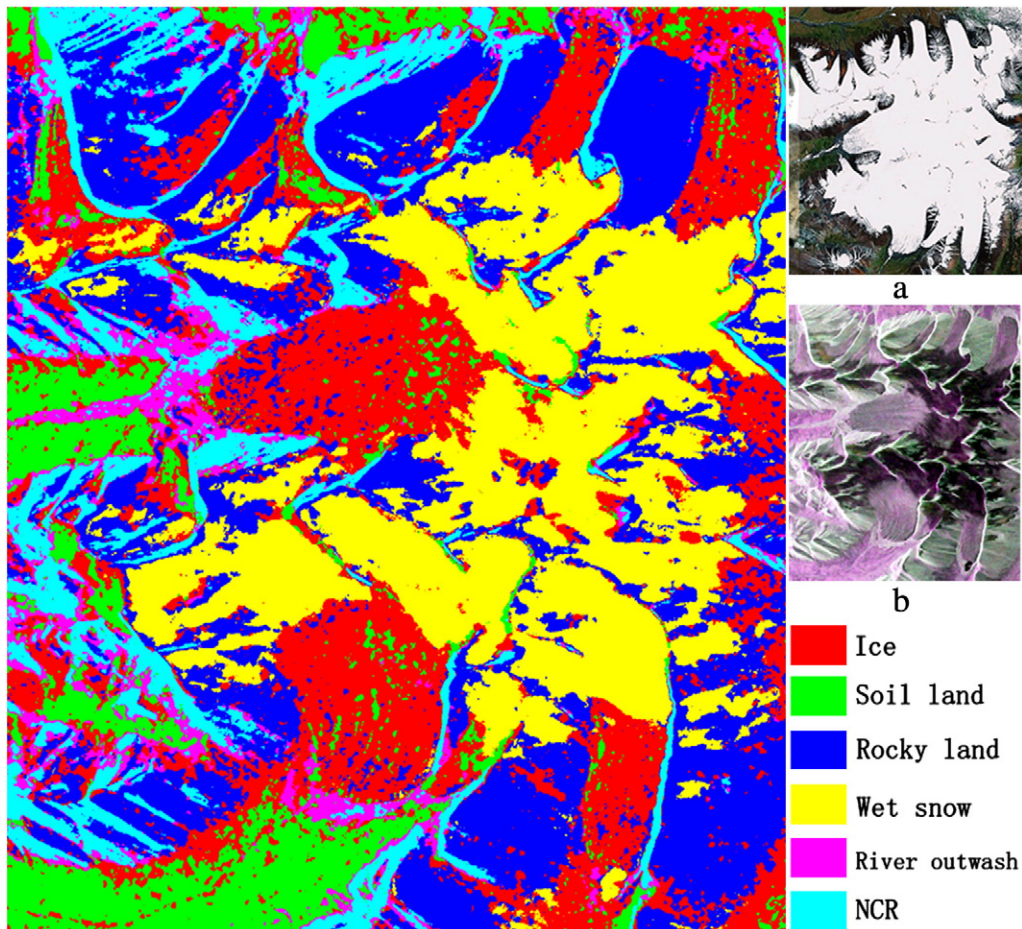


Fig. 8. The classification map obtained with the H/A/ α decomposition combined with the SVMs. Panel a is the optical image and panel b is the backscattering coefficient image of the PolSAR (HH: red, HV: green, and VV: blue). The panels a and b are given to make easier comparison of the classification map.

snow, often winter images are used to detect the position of the firn line on Greenland or polar glaciers (Storvold et al., 2004). However, in many temperate glaciers, the radar images are not useful because melting conditions also occur frequently in the winter (Jaenicke et al., 2006).

On the polarimetric SAR image, the separation between the wet snow and the ice is seen as a transition from dark to bright, where the boundary is indefinite. Because the classification is performed, and according to our definition, the snow line can theoretically be determined from the wet snow–ice boundary on the classification map. The snow line acquired on the polarimetric SAR is inherently a transient boundary. Its position and hence elevation can shift significantly on SAR images due to a heavy precipitation. For the glaciers which undergo simultaneous accumulation and ablation in the summer, summer snowfall keeps albedo high and restrains melting (Fujita & Ageta, 2000). Consequently, the snow line is still a useful parameter for many applications in hydrology and glaciology. For example, the transient position of the snow line plays a significant role in the energy balance of a glacier basin, which in turn controls the timing and quantity of melt. It is shown that during late summer, the low albedo of glacier ice and firn causes two to three times more energy to be absorbed at the surface if it were snow covered (Adam et al., 1997). In particular, the transient snow line equals the equilibrium line at the end of a balance year, and its position contains information about the mass balance (Jaenicke et al., 2006; Rau et al., 2000).

As closely related to mass balance, snow lines are in need to monitor the glaciers current ablation status. The snow lines of the major glaciers are extracted using the wet snow–ice boundary on the classification map, and the geo-rectified snow line map is shown in Fig. 9. The accuracy of the geo-rectified snow line map is within 3 pixels on glacier tongues, which corresponds to 30 m on the ground in the horizontal direction.

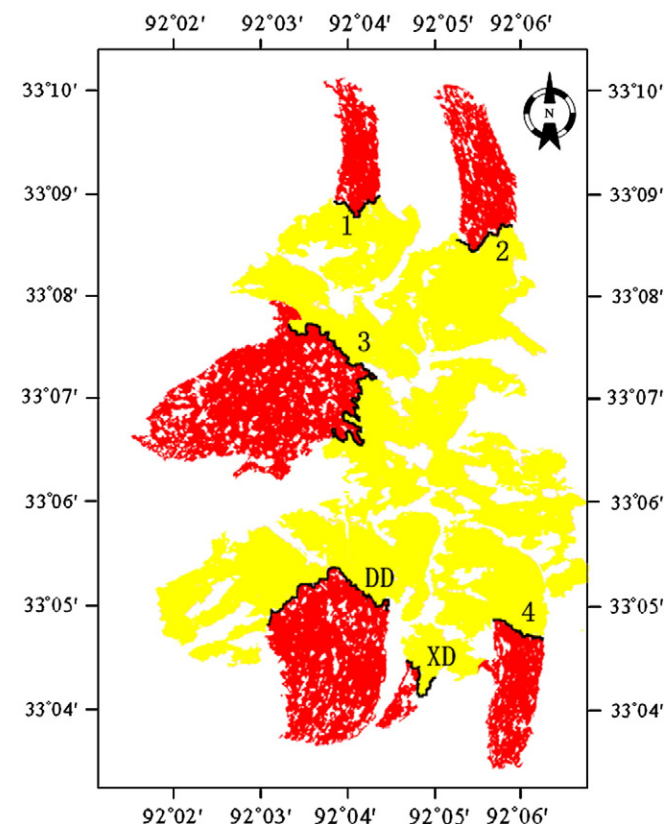


Fig. 9. The snow lines (black lines in the figure) extracted from the classification map. The major glaciers, except the DD glacier and the XD glacier, are numbered 1, 2, 3 and 4.

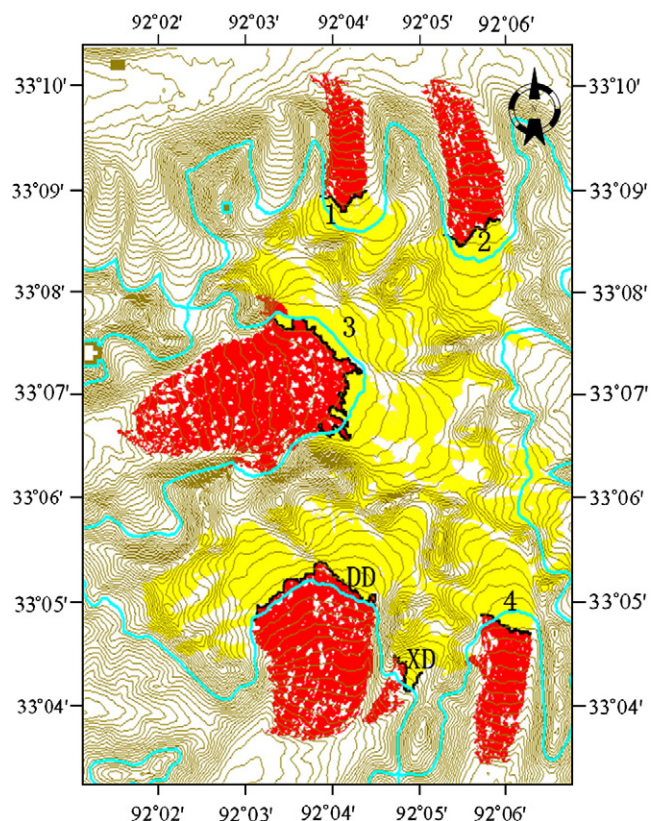


Fig. 10. Snow line map overlapped on the contour lines. The bold cyan line is the 5600 m contour line, which is used as a reference. The interval of the contour line is 20 m.

Besides the XD and DD glaciers, the major glaciers are numbered 1, 2, 3 and 4 in Fig. 9. In Fig. 10 the snow line map and the contour lines are overlapped together to show the snow line altitudes. The snow line altitudes estimated from the DEM are shown in Fig. 11. Taking the snow line altitudes together, an interesting phenomenon arises in the study area: the glaciers oriented to the south have approximately 30–60 m higher snow line altitudes than the glaciers oriented to the north, while the glacier oriented to the west have snow line altitudes in the middle. The results imply that orientation is an important factor which influences the snow line altitude of a glacier. The glaciers facing

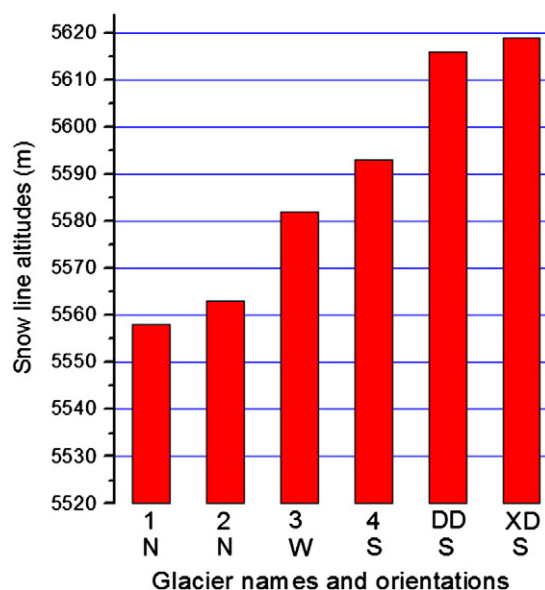


Fig. 11. The snow line altitudes, which are estimated from snow line map and the DEM.

toward the sun receive more energy, which makes it difficult to maintain the snow, and so it shrinks to a higher altitude.

5. Conclusions

The PTS method is presented for the classification of polarimetric SAR images in glacial areas. This method was developed by integrating an analysis of the polarimetric SAR scattering mechanism with a pattern recognition approach. As a feature extraction module, target decomposition derives features from the polarimetric SAR image. The SVMs classifier exploits these features for producing accurate land-cover mapping.

A detailed classification is made using the PTS method on and around the glaciers. In the study area, the image is divided into six classes: wet snow, ice, river outwash, soil land, rocky land and the natural corner reflector. The difficulty lies in the separation of the ice with the surrounding ground, which was considered indistinguishable in former research using backscattering coefficients. Within our study area, only 62.6% of the ice can be distinguished by setting thresholds among different classes. By comparing the performance in different feature spaces, we found that the ice and the ground can be better separated in the $H/A/\alpha$ decomposition feature space than in the backscattering coefficient feature space. Pauli decomposition and $H/A/\alpha$ decomposition can be combined together to better understand the scattering mechanism on the ground, though it is sufficient to perform classification only using the $H/A/\alpha$ decomposition. The following experiments verified that the $H/A/\alpha$ decomposition-based features have higher classification accuracy than the backscattering coefficient features and the Pauli decomposition features. The $H/A/\alpha$ decomposition does not only provide the scattering characteristic of the ground objects, but also provides the statistical connection between different scattering components. When using the Support Vector Machines, the accuracy was higher than when using other classifiers. The results, therefore, indicate that the combination of the $H/A/\alpha$ decomposition and the support vector machines is an accurate and efficient method for polarimetric SAR image classification in glacial areas. Using these methods, 86.63% of bare ice is correctly classified, which is about 24% higher than what is seen using traditional methods. Our method provides strong support for glacier mapping and inventory.

The PTS method is also used to determine the snow line. The snow line, which distinguishes wet snow and ice, is an important climate indicator in glaciology research. In late summer, a clear dark-to-light transition can be observed between wet snow and ice in the polarimetric SAR image of the glacier. The PTS method extracts the precise wet snow–ice boundary across the transition area, and the boundary is clear on the classification map. This method is applied to the major glaciers where the snow line altitudes are estimated. It is demonstrated that the PTS method is an effective method to detect the transient snow line on C-band polarimetric SAR images in late summer. The connection between the orientation and snow line altitude of the glacier is discussed. The extracted snow line altitude of different glaciers implies that orientation influences the snow line altitude.

Acknowledgement

The authors thank anonymous reviewers for their very helpful and constructive comments on the manuscript. Our research is supported by the Chinese Ministry of Science and Technology (Grant numbers 2009CB723901 and 2010CB951403).

References

Adam, S., Pietroniro, A., & Brugman, M. M. (1997). Glacier snow line mapping using ERS-1 SAR imagery. *Remote Sensing of Environment*, 61, 46–54.

Baghdadi, N., Gauthier, Y., & Bernier, M. (1997). Capability of multitemporal ERS-1 SAR data for wet-snow mapping. *Remote Sensing of Environment*, 60, 174–186.

Baghdadi, N., Livingstone, C. E., & Bernier, M. (1998). Airborne C-band SAR measurements of wet snow-covered areas. *IEEE Transactions on Geoscience and Remote Sensing*, 36, 1977–1981.

Camps-Valls, G., & Bruzzone, L. (2005). Kernel-based methods for hyperspectral image classification. *IEEE Transactions on Geoscience and Remote Sensing*, 43, 1–12.

Camps-Valls, G., Gomez-Chova, L., Calpe-Maravilla, J., Martin-Guerrero, J., Soria-Olivas, E., Alonso-Chorda, L., et al. (2004). Robust support vector method for hyperspectral data classification and knowledge discovery. *IEEE Transactions on Geoscience and Remote Sensing*, 42, 1530–1542.

Chen, J., Wang, C., & Wang, R. (2009). Using stacked generalization to combine SVMs in magnitude and shape feature spaces for classification of hyperspectral data. *IEEE Transactions on Geoscience and Remote Sensing*, 47, 2193–2205.

Cloude, S. R., & Pottier, E. (1996). A review of target decomposition theorems in radar polarimetry. *IEEE Transactions on Geoscience and Remote Sensing*, 34, 498–518.

Cloude, S. R., & Pottier, E. (1997). An entropy based classification scheme for land applications of polarimetric SAR. *IEEE Transactions on Geoscience and Remote Sensing*, 35, 68–78.

Engeset, R. V., & Weydahl, D. J. (1998). Analysis of glaciers and geomorphology on Svalbard using multitemporal ERS-1 SAR images. *IEEE Transactions on Geoscience and Remote Sensing*, 36, 1879–1887.

Forster, R. R., Isacks, B. L., & Das, S. B. (1996). Shuttle imaging radar (SIR-C/X-SAR) reveals near-surface properties of the South Patagonian Icefield. *Journal of Geophysical Research*, 101, 169–180.

Fujita, K., & Ageta, Y. (2000). Effect of summer accumulation on glacier mass balance on the Tibetan Plateau revealed by mass-balance model. *Journal of Glaciology*, 46, 244–252.

Fujita, K., Ageta, Y., Pu, J., & Yao, T. (2000). Mass balance of Xiao Dongkemadi glacier on the central Tibetan plateau from 1989 to 1995. *Annals of Glaciology*, 31, 159–163.

Gupta, R. P., Haritashya, U. K., & Singh, P. (2005). Mapping dry/wet snow cover in the Indian Himalayas using IRS multispectral imagery. *Remote Sensing of Environment*, 97, 458–469.

Hsu, C., Chang, C., & Lin, C. (2009). *A practical guide to support vector classification*.

Huang, C., Davis, L. S., & Townshend, J. R. G. (2002). An assessment of support vector machines for land cover classification. *International Journal of Remote Sensing*, 23, 725–749.

IPCC (2007). *Observations: Changes in snow, ice and frozen ground*. London & New York: Cambridge University Press.

Jaenicke, J., Mayer, C., Scharrer, K., Munzer, U., & Gudmundsson, A. (2006). The use of remote-sensing data for mass-balance studies at Myrdalsjokull ice cap, Iceland. *Journal of Glaciology*, 52, 565–573.

König, M., Winther, J. G., & Isaksson, E. (2001). Measuring snow and glacier ice properties from satellite. *Reviews of Geophysics*, 39, 1–27.

König, M., Winther, J. G., Knudsen, N. T., & Guneriusson, T. (2001). Firn-line detection on Austre Okstindbreen, Norway, with airborne multipolarization SAR. *Journal of Glaciology*, 47, 251–257.

Lee, J. S., Grunes, M. R., Ainsworth, T. L., Du, L. J., Schuler, D. L., & Cloude, S. R. (1999). Unsupervised classification using polarimetric decomposition and the complex Wishart classifier. *IEEE Transactions on Geoscience and Remote Sensing*, 37, 2249–2258.

Lee, J. S., & Pottier, E. (2009). *Polarimetric radar imaging: From basics to applications*. Boca Raton London New York: Taylor & Francis.

Lee, J. S., Schuler, D. L., & Ainsworth, T. L. (2000). Polarimetric SAR data compensation for terrain azimuth slope variation. *IEEE Transactions on Geoscience and Remote Sensing*, 38, 2153–2163.

Lee, J. S., Wen, J. H., Ainsworth, T. L., Chen, K. S., & Chen, A. J. (2009). Improved sigma filter for speckle filtering of SAR imagery. *IEEE Transactions on Geoscience and Remote Sensing*, 47, 202–213.

Malnes, E., & Guneriusson, T. (2002). Mapping of snow covered area with RADARSAT in Norway. *IGARSS'02. Toronto* (pp. 683–685).

Nolin, A. W., & Payne, M. C. (2007). Classification of glacier zones in western Greenland using albedo and surface roughness from the multi-angle imaging spectroradiometer (MISR). *Remote Sensing of Environment*, 107, 264–275.

Paterson, W. (1994). *The physics of glaciers*. (3rd ed.). Oxford: Elsevier Science Ltd, Chapter 4.

Pottier, E., & Lee, J. S. (1999). Application of the $H/A/\alpha$ polarimetric decomposition theorem for unsupervised classification of fully polarimetric SAR data based on the Wishart distribution. *Proc. 3rd EUSAR 2000 conference. Paris*.

Rau, F., Braun, M., Friedrich, M., Weber, F., & Goßmann (2000). Radar glacier zones and their boundaries as indicators of glacier mass balance and climatic variability. *Proceedings of EARSel-SIG-Workshop Land and Snow, Dresden* (pp. 317–327).

Rodriguez, E., Morris, C. S., & Belz, J. E. (2006). A global assessment of the SRTM performance. *Photogrammetric Engineering and Remote Sensing*, 72, 249–260.

Rott, H., & Davis, R. E. (1991). Multi-parameter airborne SAR experiments at an Alpine test site. *IGARSS'91, Espoo* (pp. 1563–1566).

Rott, H., Davis, R. E., & Dozier, J. (1992). Polarimetric and multifrequency SAR signatures of wet snow. *IGARSS'92, Houston* (pp. 1658–1660).

Rott, H., & Mätzler, C. (1987). Possibilities and limits of synthetic aperture radar for snow and glacier surveying. *Annals of Glaciology*, 9, 195–199.

RSI (2000). *RADARSAT data product specification*. Richmond: RSI-GS-026.

Salomonson, V., & Appel, I. (2004). Estimating fractional snow cover from MODIS using normalized difference snow index. *Remote Sensing of Environment*, 89, 351–360.

Shi, J., & Dozier, J. (1995). Inferring snow wetness using C-band data from SIR-C's polarimetric synthetic aperture radar. *IEEE Transactions on Geoscience and Remote Sensing*, 33, 905–914.

Shi, J., Dozier, J., & Hensley, S. (1997). Mapping snow cover with repeat pass synthetic aperture radar. *IGARSS'97. Singapore*, 2, 628–630.

- Shimoni, M., Borghys, D., Heremans, R., Perneel, C., & Acheroy, M. (2009). Fusion of PolSAR and PolInSAR data for land cover classification. *International Journal of Applied Earth Observation and Geoinformation*, 11, 169–180.
- Storvold, R., Hogda, K. A., Malnes, E., & Lauknes, I. (2004). SAR firn line detection and correlation to glacial mass balance; Svartisen glacier, northern Norway. *IGARSS'04. Anchorage (Alaska)* (pp. 1124–1127).
- Strozzi, T., Wegmuller, U., & Matzler, C. (1999). Mapping wet snowcovers with SAR interferometry. *International Journal of Remote Sensing*, 20, 2395–2403.
- Vapnik, V. (1995). *The nature of statistical learning theory*. New York: Springer-Verlag.
- Waske, B., & Linden, S. (2008). Classifying multilevel imagery from SAR and optical sensors by decision fusion. *IEEE Transactions on Geoscience and Remote Sensing*, 46, 1457–1466.